

Elastic nucleon-pion scattering amplitudes in the Δ channel at physical pion mass from lattice QCD

Constantia Alexandrou,^{1,2} Simone Bacchio^{1,2},,² Giannis Koutsou^{1,2},,² Theodoros Leontiou^{1,2,3},,³ Srijit Paul^{1,2,4},,⁴ Marcus Petschlies,⁵ and Ferenc Pittler²

¹*Department of Physics, University of Cyprus, P.O. Box 20537, 1678 Nicosia, Cyprus*

²*Computation-based Science and Technology Research Center, The Cyprus Institute, 20 Kavafi Street, Nicosia 2121, Cyprus*

³*Frederick Research Center, 7 Filokyprou Street Palouriotissa, 1036 Nicosia, Cyprus*

⁴*Higgs Center for Theoretical Physics, The University of Edinburgh, Peter Guthrie Tait Road, Edinburgh EH9 3FD, United Kingdom*

⁵*HISKP (Theory), Rheinische Friedrich-Wilhelms-Universität Bonn, Nußallee 14-16, 53115 Bonn, Germany*



(Received 7 August 2023; accepted 17 January 2024; published 15 February 2024)

We present an investigation of pion-nucleon elastic scattering in the $I(J^P) = \frac{3}{2}(\frac{3}{2}^+)$ channel using lattice QCD with degenerate up and down, strange and charm quarks with masses tuned to their physical values. We use an ensemble of twisted mass fermions with box size $L = 5.1$ fm and lattice spacing $a = 0.08$ fm and we consider the πN system in rest and moving frames up to total momentum $\vec{P}^2 = 3(2\pi/L)^2 = 0.17$ GeV². We take into account the finite volume symmetries and S - and P -wave mixing, and use the Lüscher formalism to simultaneously constrain the $J = 1/2, \ell = 0$ and $J = 3/2, \ell = 1$ scattering amplitudes. We estimate the Δ resonance pole in the P -wave channel as well as the S -wave isospin-3/2 scattering length.

DOI: [10.1103/PhysRevD.109.034509](https://doi.org/10.1103/PhysRevD.109.034509)

I. INTRODUCTION

The precise treatment of nucleon resonances is still a formidable task in lattice QCD. While Lüscher's method [1–3] is the established theoretical basis for connecting observed lattice QCD spectra to scattering amplitudes, thus allowing the investigation of properties of bound states and resonances from first principles, in practice the study of meson-baryon, two-hadron states remains challenging. This is especially so when using simulations with physical values of the light quark mass, which carry increased statistical errors.

Nevertheless, the *ab initio* computation of low-energy elastic pion-nucleon (πN) scattering from lattice QCD is essential for the study of nucleon interactions, and any such treatment necessarily starts with the lowest-lying meson-baryon resonance, namely the $I(J^P) = \frac{3}{2}(\frac{3}{2}^+)$ Δ P -wave resonance. The Δ resonance governs nucleon-pion, nucleon-photon, and nucleon-neutrino scattering as the dominant channel. Within the lattice QCD formalism, excited state contributions from pion-nucleon scattering states dominate

the spectrum in nucleon form factor calculations in a finite volume for gauge ensembles generated with close to physical pion mass [4,5].

The interaction of nucleon and pion has been studied by various approaches in lattice QCD in the past, using gauge ensembles generated with heavier-than-physical pion masses. Nucleon-pion scattering amplitudes and the Δ in particular have been the subject of Refs. [6–13] using the Lüscher method. References [14,15] used an alternative method based on Refs. [16,17]. There are also studies using ensembles generated with quark masses at which the Δ is a stable state [18–23].

With this work, we extend the lattice calculation of the Δ from heavier-than-physical to physical pion mass, and explore the application of the Lüscher method to the $\pi N - \Delta$ channel at the physical point. We estimate the Δ resonance pole in the P -wave channel as well as the S -wave isospin-3/2 scattering length, which experimentally enters the evaluation of the pion-nucleon σ -term using the Roy-Steiner-equations. For this first physical point calculation, we use a single ensemble with two degenerate light quarks, strange, and charm quarks ($N_f = 2 + 1 + 1$).

The paper is organized as follows: In Sec. II, we describe our application of the Lüscher method, with further details on the implementation of the lattice spectroscopy in Sec. III. Sections IV and V present our analysis of the lattice data for the $\pi N - \Delta$ spectrum, and subsequent fits to

Published by the American Physical Society under the terms of the Creative Commons Attribution 4.0 International license. Further distribution of this work must maintain attribution to the author(s) and the published article's title, journal citation, and DOI. Funded by SCOAP³.

the finite-volume quantization condition. In addition, we use the threshold expansion of the Lüscher quantization condition to determine the S -wave scattering length. A discussion of the results and concluding remarks are given in Sec. VI. In Appendixes A–C we include extended figures and tables of our results, as well as some additional details of our analysis.

II. LATTICE QCD FORMALISM FOR PION-NUCLEON SCATTERING

We consider elastic scattering of two particles of non-equal mass and with spin in a hypercubic box of spatial extent L . The constraints on infinite-volume scattering amplitudes from the finite volume lattice spectrum for this setup are given in Lüscher’s original work [1–3] and a series of extensions, to moving frames [24,25], to nondegenerate particles [26] and to particles with spin [27–30]. While the formalism for multiple coupled two-particle decay channels is also known [31,32], for the purposes of this work we perform a single decay channel analysis, since the expected branching fraction $\Delta \rightarrow \pi N$ is almost 100% making this channel a prototype application for lattice QCD.

The finite-volume method for three particles has been further developed for spinless particles [33–36]. For the $N\pi\pi$ system a formalism is not yet available, and we thus only consider the πN interaction here. We will define an upper limit to the spectrum entering our elastic scattering amplitude fits, such that the impact of the three-particle scattering is negligible.

For the pion-nucleon system, even and odd partial waves mix. Moreover, the spin of the nucleon couples to the orbital angular momentum, such that in the finite-volume analysis the most relevant partial wave amplitudes are $J = 1/2$, containing S - and P -wave, and $J = 3/2$, with P - and D -wave. The $J = 3/2$ P -wave amplitude corresponds to the Δ resonance and is expected to dominate, with a sub-leading contribution from $J = 1/2$ S -wave, while amplitudes from the corresponding higher ℓ values are suppressed by angular momentum barrier.

To the extent described above, the Lüscher quantization conditions have been given in detail in Refs. [30,37] with the master equation given by

$$\det \left(M_{J\ell n; J'\ell' n'}^{\vec{P}, \Lambda} - \delta_{JJ'} \delta_{\ell\ell'} \delta_{nn'} \cot(\delta_{J\ell}) \right) = 0, \quad (1)$$

where $M^{\vec{P}, \Lambda}$ denotes the reduced Lüscher finite volume matrix for a reference frame with total momentum \vec{P} of the πN system, and for irreducible representation (irrep) Λ of the little group $LG(\vec{P}) \subseteq O_h^D$. Here we use the reduced Lüscher matrices and quantization conditions from Refs. [30,37]. The determinant is taken in the linear space of total angular momentum J , J' , orbital angular momentum ℓ , ℓ' and multiplicity (or occurrence) of the irrep Λ , n , n' .

For ensembles with physical value of the pion mass, the thresholds for elastic nucleon-pion scattering are given by $E_{2\text{-thr}} = m_N + m_\pi \approx 1080$ MeV and the three-particle threshold $E_{3\text{-thr}} = m_N + 2m_\pi \approx 1220$ MeV. The correspondingly narrow window in the center-of-mass energy for elastic πN scattering does not cover the expected resonance region and puts prohibitive cuts on the usable finite-volume lattice spectrum. However, based on experimental observations, the πN scattering amplitude in the $I = 3/2$ channel is vastly dominated by the elastic two-particle interaction up to $E'_{3\text{-thr}} = m_\Delta + m_\pi$ as a proxy three-particle threshold, where the Δ and the pion can propagate on shell [38]. We thus consider lattice energy levels up to $\sqrt{s} \lesssim E'_{3\text{-thr}} \approx 1360$ MeV.

The partial wave amplitudes are parametrized via the associated phase shifts. In particular, for the considered leading phase shifts $\delta_{J\ell}$, we employ the analytic Breit-Wigner form for the resonant Δ channel and the leading-order effective range expansion with isospin $I = 3/2$ S -wave scattering length a_0 ,

$$\cot(\delta_{\frac{1}{2}0}(s)) = a_0 q_{\text{cmf}}, \quad (2)$$

$$\tan(\delta_{\frac{3}{2}1}(s)) = \frac{\sqrt{s} \Gamma(\Gamma_R, M_R, s)}{M_R^2 - s}. \quad (3)$$

The center-of-mass momentum (q_{cmf}) of the πN system is given by

$$q_{\text{cmf}}^2(s) = \frac{(s - M_N^2 - M_\pi^2)^2 - 4M_N^2 M_\pi^2}{4s}, \quad (4)$$

and the resonance decay width has invariant mass dependence parametrized by

$$\Gamma(\Gamma_R, M_R, s) = \Gamma_R \left(\frac{q_{\text{cmf}}(s)}{q_{\text{cmf}}(M_R^2)} \right)^3 \frac{M_R^2}{s}. \quad (5)$$

III. CORRELATION MATRIX CONSTRUCTION

A. Interpolating operators

To constrain pion-nucleon scattering amplitudes using the Lüscher method, we determine the low-lying finite-volume energy spectrum of the lattice Hamiltonian with isospin $I = 3/2$. The operator basis for the correlation matrices of two-point functions is constructed from single- and two-hadron time slice interpolating operators. We consider the case of maximal isospin, i.e. $I_3 = +3/2$, meaning we use the Δ^{++} , and the proton and charged pion (N^+ and π^+).

The single-hadron, quark model Δ -type interpolating operator reads

$$(O_{\Delta^{++}})_{\alpha,k}(\vec{P}; t) = \sum_{\vec{x}} \varepsilon_{abc} u_{\alpha}^a(\vec{x}, t) [u^b(\vec{x}, t)^{\top} \mathcal{C} \gamma_k u^c(\vec{x}, t)] e^{i\vec{P}\vec{x}},$$

$$k = x, y, z. \quad (6)$$

The two-hadron interpolators are generated by products of nucleon and pion interpolators given by

$$(O_{N^+\pi^+})_{\alpha}(\vec{p}_N, \vec{p}_{\pi}; t) = N_{\alpha}^+(\vec{p}_N; t) \pi^+(\vec{p}_{\pi}; t), \quad (7)$$

with

$$N_{\alpha}^+(\vec{p}; t) = \sum_{\vec{x}} \varepsilon_{abc} u_{\alpha}^a(\vec{x}, t) [u^b(\vec{x}, t)^{\top} \mathcal{C} \gamma_5 d^c(\vec{x}, t)] e^{i\vec{p}\vec{x}}, \quad (8)$$

$$\pi^+(\vec{p}, t) = \sum_{\vec{x}} \bar{d}(\vec{x}, t) \gamma_5 u(\vec{x}, t) e^{i\vec{p}\vec{x}}, \quad (9)$$

where u and d are up- and down-quark spinor fields, $\mathcal{C} = \gamma_4 \gamma_2$ is the charge-conjugation matrix, and α denotes the spinor index. The total momentum of such interpolating fields is $\vec{P} = \vec{p}_N + \vec{p}_{\pi}$.

The above operators are projected to irreducible representations of the lattice rotation symmetry groups [O_h^D for $\vec{P} = 0$ or little group $LG(\vec{P})$] for the rest and moving frames. The values of the total momenta \vec{P} and lattice irreps used are given in Table I, where we also indicate the subduced angular momenta.

The projection to irrep Λ , row r for occurrence n , follows from the group theory master formula, namely for the single hadron operators O_{Δ} and the πN operators $O_{\pi N}$ we use

$$O_{\Delta;\alpha,k}^{\Lambda,r,n}(\vec{P})^{\dagger} = \frac{\dim(\Lambda)}{\#LG(\vec{P})} \sum_{G \in LG(\vec{P})} \Gamma^{\Lambda}(G)_{r,r'}^* U^{(1)}(G)_{k',k} U^{(1/2\oplus 1/2)}(G)_{\alpha',\alpha} \Delta_{\alpha',k}(\vec{P})^{\dagger},$$

$$O_{N\pi;\alpha}^{\Lambda,r,n}(\vec{P}, \vec{p})^{\dagger} = \frac{\dim(\Lambda)}{\#LG(\vec{P})} \sum_{G \in LG(\vec{P})} \Gamma^{\Lambda}(G)_{r,r'}^* U^{(1/2\oplus 1/2)}(G)_{\alpha',\alpha} \bar{N}_{\alpha'}(R\vec{p}) \pi(\vec{P} - R\vec{p})^{\dagger}, \quad (10)$$

where the group element $G \in LG(\vec{P})$ means either a proper rotation R or a rotation-inversion IR , such that $R\vec{P} = -\vec{P}$ and concatenation with spatial inversion I leaves invariant \vec{P} . Analogously, $U^{(J)}(G)$ denotes the $SU(2)$ spin- J representation matrix of the proper rotation or rotation-inversion group element. The rotation matrix $U^{(1)}$ acting on the momentum vector \vec{p} in Cartesian basis, is denoted as R for simplicity. Moreover, $\Delta_{\alpha,k}$ and N_{α} are Dirac four-spinors and the rotation matrix for the four-component spinors is denoted as $U^{(1/2\oplus 1/2)}$. The space inversion operation $(\vec{x}, t) \rightarrow (-\vec{x}, t)$ is represented by $\pi^+(\vec{x}, t) \rightarrow -\pi^+(-\vec{x}, t)$ for the pseudoscalar pion field, and by $\Delta_{\alpha,k}(\vec{x}, t) \rightarrow (\gamma_4)_{\alpha\beta} \Delta_{\beta,k}(-\vec{x}, t)$ for the four-component nucleon and Δ spinors.

The constructed set of irrep-projected operators $\{O_{\Delta;\alpha,k}^{\Lambda,r,n}(\vec{P}), O_{N\pi;\alpha}^{\Lambda,r,n}(\vec{P}, \vec{p})\}$ is still linearly dependent and we extract a basis set by the Gram-Schmidt procedure. The orthogonalization is done with respect to the tensor components α, k and momentum vector \vec{p} .

B. Equivalent moving frames

The explicit subduction coefficients for the operators, which are obtained based on the convention in Ref. [39], pertain to the reference moving frames with total momentum $\vec{P}/(2\pi/L) = (0, 0, 1), (0, 1, 1), (1, 1, 1)$. We include lattice correlation functions also from all other equivalent moving frames of the same orbit as \vec{P} under discrete

TABLE I. Momentum frames (first column), lattice rotation symmetry groups (second column) and irreducible representations Λ (third, fourth, and fifth columns) with their subduced angular momentum content J , relevant for the pion ($J^P = 0^-$), the nucleon ($J^P = 1/2^+$), and the Δ -baryon ($J^P = 3/2^+$). The naming of irreps follows Ref. [39].

$\vec{P}[2\pi/L]$	$LG(\vec{P})$	I		
		1	1/2	3/2
(0,0,0)	O_h^D	$A_{1u}(0^-, 4^-, \dots)$	$G_{1g}(1/2^+, 7/2^+, \dots)$	$H_g(3/2^+, 5/2^+, \dots)$
(0,0,1)	C_{4v}^D	$A_1(0, 1, \dots)$	$G_1(1/2, 3/2, \dots)$	$G_1(1/2, 3/2, \dots) G_2(3/2, 5/2, \dots)$
(0,1,1)	C_{2v}^D	$A_1(0, 1, \dots)$	$G(1/2, 3/2, \dots)$	$G(1/2, 3/2, \dots) G(1/2, 3/2, \dots)$
(1,1,1)	C_{3v}^D	$A_1(0, 1, \dots)$	$G(1/2, 3/2, \dots)$	$F_1(3/2, 5/2, \dots) F_2(3/2, 5/2, \dots)$

TABLE II. Rotation group elements (R) to map moving frames \vec{P}' to their reference directions. The first set of two columns correspond to reference moving frame $\vec{P}/(2\pi/L) = (0, 0, 1)$, the second to $(0, 1, 1)$, and the third set to $(1, 1, 1)$. The superscript i denotes the inverse group element.

$\vec{P}'/(2\pi/L)$	R	$\vec{P}'/(2\pi/L)$	R	$\vec{P}'/(2\pi/L)$	R
$(0, 1, 0)$	C_{4x}^i	$(1, -1, 0)$	C_{2c}	$(1, 1, -1)$	C_{4y}
$(1, 0, 0)$	C_{4y}	$(1, 0, 1)$	C_{4z}^i	$(1, -1, 1)$	C_{4x}
$(0, 0, -1)$	C_{2a}	$(1, 0, -1)$	C_{2a}	$(-1, 1, 1)$	C_{4y}^i
$(0, -1, 0)$	C_{4x}	$(1, 1, 0)$	C_{4y}	$(1, -1, -1)$	C_{2x}
$(-1, 0, 0)$	C_{4y}^i	$(0, 1, -1)$	C_{4x}^i	$(-1, 1, -1)$	C_{2y}
		$(0, -1, 1)$	C_{4x}	$(-1, -1, 1)$	C_{2z}
		$(0, -1, -1)$	C_{2f}	$(-1, -1, -1)$	C_{2b}
		$(-1, 0, -1)$	C_{2b}		
		$(-1, 0, 1)$	C_{4z}		
		$(-1, -1, 0)$	C_{2d}		
		$(-1, 1, 0)$	C_{4y}^i		

rotations. Little groups $LG(\vec{P}')$ and $LG(\vec{P})$ with $\vec{P}^2 = \vec{P}'^2$ are equivalent for the values considered here, namely $\{\vec{P}^2 \leq 3(2\pi/L)^2\}$, and we select one group element $R_{\vec{P}'} \in O_h^D$ per case, which relates $\vec{P}' = R_{\vec{P}'} \vec{P}$.

These lattice correlators are mapped to the reference moving frame by the corresponding $SU(2)$ J -representation of the source and sink operators. The specific choices of group elements for the mapping are given in Table II. The residual moving frames are related to the reference frames and those listed in Table II by momentum inversion. The corresponding operators and lattice correlators are thus mapped by the parity transformation I .

C. Contractions

Our method to compute correlation functions of single- and two-particle operators efficiently is based on the factorization of the quark flow diagrams [7]. We show the diagrams that contribute to the $N\pi - N\pi$ two-point function in Fig. 1.

The colors used for the different propagators shown in Fig. 1 denote the method used to evaluate them. We denote spinor indices by lower case Greek indices, whereas color indices are lower case Latin indices.

In particular, point-to-all propagators (S) denoted with red lines read,

$$S_{\alpha,\beta}^{a,b}(x; x_i) = D^{-1}_{\alpha,\gamma}{}^{a,b}(x; x_i) \quad \text{---} \quad (11)$$

where x_i , β , and b are the coordinates, Dirac index, and color index of the source, respectively. Sequential propagators (T) are denoted with blue lines and are given by

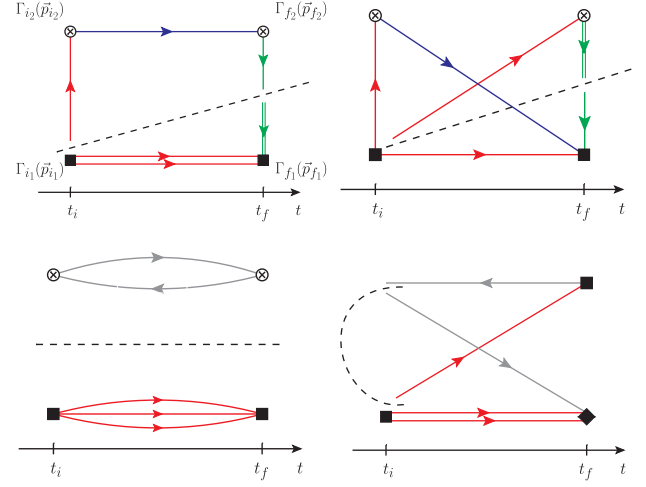


FIG. 1. Different types of diagrams showing the contractions of the cost-intensive πN correlation functions. The dashed line shows the applied splitting into diagram factors. As explained in more detail in the text, point-to-all propagators are denoted with red lines, sequential propagators with blue lines, stochastic sources (propagators) with single (double) green lines, and one-end-trick stochastic propagator pairs with gray lines.

$$T_{\alpha,\beta}^{a,b}(x; t_{\text{seq}}, \vec{p}_{\text{seq}}; x_i) = D^{-1}_{\alpha,\gamma}{}^{a,c}(x; y) \times \left[(\Gamma_{\text{seq}})_{\gamma\gamma'} e^{i\vec{p}_{\text{seq}}\vec{y}} S_{\gamma',\beta}^{c,b}(t_{\text{seq}}, \vec{y}; x_i) \right] \quad \text{---} \quad (12)$$

constructed from an inversion of the Dirac operator using a point-to-all propagator as a source vector (also referred to as the sequential source) with support on time slice t_{seq} and with a vertex given by Dirac structure Γ_{seq} and three-momentum insertion \vec{p}_{seq} .

The stochastic sources (η) and propagators (ϕ) are denoted with green single and double lines respectively,

$$\phi_{\alpha,a}^r(x) \eta_{\beta,b}^r(y)^* = D^{-1}_{\alpha,\gamma}{}^{a,c}(x; z) \times \left[\eta_{\gamma,c}^r(z) \eta_{\beta,b}^r(y)^* \right] \quad \text{---} \quad (13)$$

where $\eta_{\alpha,a}^r(x)$ are sources with $Z_2 \times iZ_2$ independent and identically distributed (iid) noise of zero mean and unit variance,

$$\begin{aligned} \mathbb{E}[\eta_{\gamma,c}^r(z)] &= 0, \\ \mathbb{E}[\eta_{\gamma,c}^r(z) \eta_{\beta,b}^r(y)^*] &= \delta_{\gamma,\beta} \delta_{c,b} \delta_{z,\vec{y}} \delta_{t_z,t_y}. \end{aligned} \quad (14)$$

The expectation value $\mathbb{E}[\cdot]$ is taken over the stochastic noise index r . In practice, we use time slice noise sources, i.e. sources with support on a single time slice, $\eta_{\alpha,a}^{(r;t_0)}(x) = \eta_{\alpha,a}^r(x) \delta_{t_x,t_0}$. The gray, one-end-trick propagators, are

constructed using spin-diluted $Z_2 \times iZ_2$ stochastic time slice sources, appropriately multiplied by a momentum phase, $\eta_{\alpha,a}^{(r;t_0;\mu;\vec{p})}(x) = \eta_{\alpha,a}^r(x) \delta_{t_x,t_0} \delta_{\alpha,\mu} e^{i\vec{p}\cdot\vec{x}}$ and solution vectors ϕ indicated as $\phi_{\beta,b}^{(r;t_0;\mu;\vec{p})}(y) = D^{-1}_{\beta,a}(y;x) \eta_{\alpha,a}^{(r;t_0;\mu;\vec{p})}(x)$,

$$\phi_{\alpha,a}^{(r;t_{\text{seq}};\kappa;\vec{p}_{\text{seq}})}(x) (\Gamma_{\text{seq}} \gamma_5)_{\kappa\lambda} \phi_{\beta',b}^{(r;t_{\text{seq}};\lambda;0)}(y)^* (\gamma_5)_{\beta'\beta} \quad \leftarrow \otimes \leftarrow \quad (15)$$

Analogous to Eq. (14), the source components are iid with $Z_2 \times iZ_2$ noise and have zero mean and unit variance.

The diagrams in Fig. 1 are further split into products of building blocks. These cuts are illustrated by the dashed lines. The quark connected diagrams are split at the source point by virtue of spin-color dilution, and by the stochastic decomposition of unity with the stochastic sources and propagators in Eqs. (13) and (15), schematically $\eta\eta^\dagger \approx 1$. The factors are two- and three-fold propagator products, which are partially reduced in spin-color space and momentum projected at the pion vertex labeled f_2 in Fig. 1 and the nucleon vertex f_1 . Each type of the four diagrams depicted represents several combinations of contractions, and thus by the factorization multiple contractions benefit from sharing a small number of common factors.

The Wick contractions for $\Delta - \Delta$ and $\Delta - N\pi$ two-point functions are not found to significantly benefit from this factorization and are therefore calculated from point-to-all and point-to-all plus sequential propagators, respectively.

Both the computation of building blocks and their subsequent recombination to full correlation functions is carried out on GPUs using the PLEGMA software package [40].

D. Quark field smearing

We apply Gaussian smearing [41] to the source and sink for all quark propagators. The smearing parameters are $N_{\text{Gauss}} = 140$ steps with weight $\alpha_{\text{Gauss}} = 1$. The gauge links entering the Gaussian smearing kernel are APE-smear [42] with $N_{\text{APE}} = 50$ steps and weight $\alpha_{\text{APE}} = 0.4$. The parameters α_{Gauss} and N_{Gauss} are tuned in order to approximately give a smearing radius for the nucleon of 0.5 fm. Δ ground state energy in the center-of-mass frame, as a function of the smearing parameters confirmed that these values were appropriate.

E. Gauge ensemble and statistics

We use a gauge ensemble generated by the Extended Twisted Mass Collaboration [43] with two degenerate light quarks with twisted mass parameter tuned to reproduce the pion mass and the strange and charm quarks ($N_f = 2 + 1 + 1$) with masses tuned close to their physical values by matching the kaon meson mass and the ratio of renormalized quark masses $m_c/m_s|_{\overline{\text{MS}},\mu=2 \text{ GeV}}$, respectively.

TABLE III. Parameters of the ensemble cB211.072.64 used in this work.

$L^3 \times T$	a [fm]	L [fm]	M_π [MeV]	$M_\pi L$	M_N [MeV]
$64^3 \times 128$	0.0801	5.1	139.43(9)	3.6	944(10)

TABLE IV. Statistics used in this work. We indicate the number of configurations used (N_{conf}), and per configuration, the number of source points (N_{src}) for point-to-all propagators, the number of stochastic time slice sources (N_{stoch}), and the number of stochastic one-end-trick sources (N_{oet}).

N_{conf}	N_{src}	N_{stoch}	N_{oet}	Subset
400	256	12	1	$N - N$, $\pi N - \pi N$ with $\vec{p}_\pi = \vec{p}_N = 0$
400	64	12	1	All other correlation functions and kinematic setups

The fermion action is given by twisted mass fermions at maximal twist with the addition of a Sheikholeslami-Wohlert ‘‘clover’’ term. The gluon action is the Iwasaki gauge action. The parameters of the ensemble, denoted as ‘‘cB211.072.64,’’ are collected in Table III.

We use $N_{\text{conf}} = 400$ well-separated gauge configurations and on each configuration generate correlation functions from multiple source positions (N_{src}) to increase statistics. In general, we use 64 sources per configuration ($N_{\text{src}} = 64$), except for the specific cases of the nucleon to nucleon ($N - N$) two-point correlation function and the pion-nucleon to pion-nucleon ($\pi N - \pi N$) two-point correlation function with both pion and nucleon at rest, for which we use increased statistics of $N_{\text{src}} = 256$. More details of the statistics, including the stochastic sources used, are provided in Table IV.

IV. SPECTRAL ANALYSIS

A. Correlator matrices, fits and excited state identification

We build real symmetric correlation matrices $C_{ij}(t) = \langle O_i(t) O_j(t_0)^\dagger \rangle$, where $O_i(t)$ are the correlation functions after projecting to the lattice symmetry group, Eq. (10). For extracting the energy levels from the correlation matrices, we use four methods, which we detail in what follows.

1. Generalized eigenvalue problem

In what we will refer to as the *GEVP method*, we solve the so-called generalized eigenvalue problem (GEVP) [44,45] for the matrix of correlation functions

$$C_{ij}(t) v_j^n(t_0) = C_{ij}(t_0) v_j^n(t_0) \lambda^n(t, t_0), \quad (16)$$

where $v_j^n(t)$ is the j th component of the n th eigenvector on time slice t and $\lambda^n(t, t_0)$, the n th eigenvalue of this GEVP,

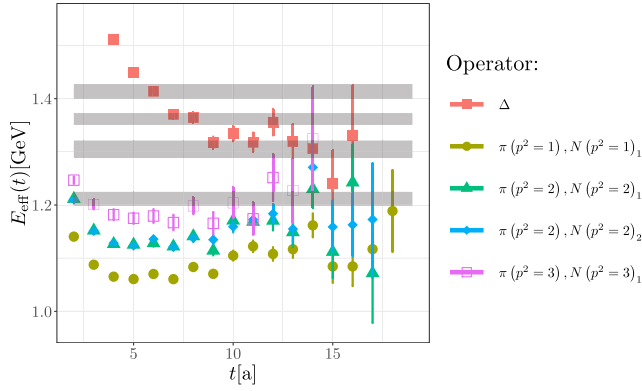


FIG. 2. The effective mass from each diagonal correlator in the center-of-mass frame H_g correlation matrix, using a 5×5 basis of interpolating operators listed in the legend. The gray bands show the energy levels obtained by the GEVP analysis.

referred to as the principal correlator. In order to obtain energy eigenvalues, we fit the principal correlator to a single-exponential form

$$f_1(t, t_0) = A_1 e^{-E(t-t_0)}, \quad t \in [t_{\min}, t_{\max}]. \quad (17)$$

An example of the analysis using GEVP is shown in Fig. 2, where we plot the effective masses $m_{\text{eff}}^i = \log \frac{C_{ii}(t)}{C_{ii}(t+1)}$ of the diagonal elements of the correlation matrix for the case of the center-of-mass frame H_g . The five interpolating operators, that include four momentum combinations of πN and one Δ , are indicated in the legend.

2. Prony generalized eigenvalue method

We apply the Prony generalized eigenvalue method [46,47] directly on the principal correlators obtained via the GEVP method. In PGEVM, we solve the second-level GEVP for the correlation matrix $C^{(2)}$ defined by λ^n as

$$C_{ij}^{(2)}(t) = \begin{pmatrix} \lambda^n(t, t_0) & \lambda^n(t+1, t_0) \\ \lambda^n(t+1, t_0) & \lambda^n(t+2, t_0) \end{pmatrix}_{ij}. \quad (18)$$

While with the GEVP method the stability of the ground state from λ^n is tested by a conservative choice of t_{\min} , with PGEVM a second, consecutive ground-state projection is applied, which is expected to lead to an earlier onset of ground state dominance and thus smaller statistical errors.

3. Athens model-independent analysis scheme

In the Athens model-independent analysis scheme (AMIAS) method [48] we perform multistate fits directly to the correlation matrix. Namely, the spectral decomposition of the correlation functions $C_{ij}(t) = \sum_{n=1}^{n_{\max}} A_n^{(ij)} e^{-E_n t}$ is used to construct the χ^2 function

$$\chi^2 = \sum_{j,k} \sum_{t=t_{\min}}^{t_{\max}} \frac{(C_{jk}(t) - \sum_{n=1}^{n_{\max}} A_n^{(jk)} e^{-E_n t})^2}{\sigma_{jk}^2}, \quad (19)$$

where the amplitudes, $A_n^{(jk)}$ and the energies, E_n , are fit parameters and n_{\max} is used to truncate the spectral expansion. The probability distribution function (PDF) for the complete set of parameters is $p(A, E) = \frac{1}{Z} e^{-\chi^2/2}$, where the normalization factor $Z = \int \prod_{n=1}^{n_{\max}} dA_n dE_n e^{-\chi^2/2}$. The estimates for the values of the fit parameters and their uncertainties are then obtained as the expectation values and the standard deviations of the corresponding PDF,

$$\bar{E}_k = \int \prod_{n=1}^{n_{\max}} dA_n dE_n E_k p(E, A), \quad (20)$$

$$\sigma^2(E_k) = \int \prod_{n=1}^{n_{\max}} dA_n dE_n (E_k^2 - \bar{E}_k^2) p(E, A). \quad (21)$$

These integrals are computed using standard Monte Carlo methods. In AMIAS, one investigates the behavior of the distributions of the fit parameters of the lower states of interest as the truncation parameter n_{\max} is increased.

As demonstrated in previous applications of this method [48–50], at large values of n_{\max} , the additional parameters added, to which χ^2 is insensitive, become irrelevant in the integrals of Eq. (21) and thus the distributions of the energies of interest converge, without loss of accuracy. In this way larger fit intervals $[t_{\min}, t_{\max}]$ (i.e. smaller t_{\min}) can be probed.

An example application of AMIAS is shown in Fig. 3, where the distributions of the energy levels for the case of the G_1 irrep are plotted. As can be seen, using $n_{\max} = 5$ all five energy levels are clearly distinguishable. A similar analysis is carried out for the amplitudes $A_n^{(ij)}$ and for all irreps considered, to obtain the mean values and errors of

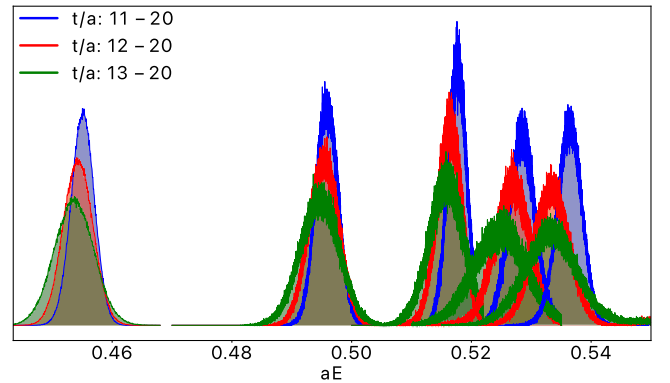


FIG. 3. Results on the energy spectrum for the G_1 irrep using the AMIAS method. We show the distributions for the energies when $t_{\min}/a = 11$ (blue curves), 12 (red curves), and 13 (green curves). The correlation matrix is the same as in the 5×5 problem used in Fig. 2.

these parameters via Eq. (21). All results in this work quoted as using the AMIAS method used up to $n_{\max} = 4$.

4. Ratio method

Following Ref. [51] we take the principal correlator from the GEVP analysis, and fit the energy shift with respect to a given noninteracting energy level. In practice this is done by taking the ratio of the principal correlator $\lambda^n(t, t_0)$ from Eq. (16) to the product of single hadron correlation functions with the appropriate momenta, given by

$$C_{\vec{p}_N, \vec{p}_\pi}^R(t) = \frac{\lambda^{\vec{P}, \Lambda, n}(t, t_0)}{C_N(t, \vec{p}_N) \cdot C_\pi(t, \vec{p}_\pi)}, \quad (22)$$

$$\vec{P} = \vec{p}_N + \vec{p}_\pi.$$

We will refer to this approach as the *ratio method*. The leading energy dependence of the ratio in Eq. (22) follows as

$$C_{\vec{p}_N, \vec{p}_\pi}^R(t) \stackrel{\text{large } t}{\propto} \frac{e^{-E^{\vec{P}, \Lambda, n} t}}{e^{-E^{\vec{p}_N, \Lambda_N, 0} t} e^{-E^{\vec{p}_\pi, \Lambda_\pi, 0} t}} = e^{-(E^{\vec{P}, \Lambda, n} - E^{\vec{p}_N, \Lambda_N, 0} - E^{\vec{p}_\pi, \Lambda_\pi, 0}) t} = e^{-\Delta E^{\vec{P}, \Lambda, n}(\vec{p}_N, \vec{p}_\pi) t}, \quad (23)$$

where $E^{\vec{p}_N, \Lambda_N, 0}$ and $E^{\vec{p}_\pi, \Lambda_\pi, 0}$ are the ground-state energy of the nucleon and pion two-point function in the relevant irreps, respectively. Taking the ratio reduces substantially the excited state contribution in a given principal correlator, and especially for small energy shifts $\Delta E^{\vec{P}, \Lambda, n}(\vec{p}_N, \vec{p}_\pi)$ allows to determine the latter with significantly increased statistical precision. For large t the logarithm of $C^R(t)$ will converge to a linear function, with the slope corresponding to the energy shift $\Delta E^{\vec{P}, \Lambda, n}(\vec{p}_N, \vec{p}_\pi)$ relative to the noninteracting πN energy,

$$\log(C_{\vec{p}_N, \vec{p}_\pi}^R(t)) \stackrel{\text{large } t}{\propto} \text{const} - \Delta E^{\vec{P}, \Lambda, n}(\vec{p}_N, \vec{p}_\pi) \cdot t. \quad (24)$$

An example of such an analysis is shown in Fig. 4, for the case of the H_g irrep, which corresponds to the center-of-mass frame with total momentum zero (see Table I). The ratio is applied to the πN case for three different relative momenta \vec{p}_N, \vec{p}_π between the nucleon and pion. From the energy shift obtained by the slope, we reconstruct the interacting two-hadron energy level by shifting back the energies using the continuum dispersion relation,

$$E^{\vec{P}, \Lambda, n} = \Delta E^{\vec{P}, \Lambda, n}(\vec{p}_N, \vec{p}_\pi) + \sqrt{m_N^2 + \vec{p}_N^2} + \sqrt{m_\pi^2 + \vec{p}_\pi^2}. \quad (25)$$

Equation (25) has the added advantage, that high-precision estimates for the nucleon and pion mass can be employed.

Using different single-hadron momenta for pion and nucleon with same total momentum to determine the same

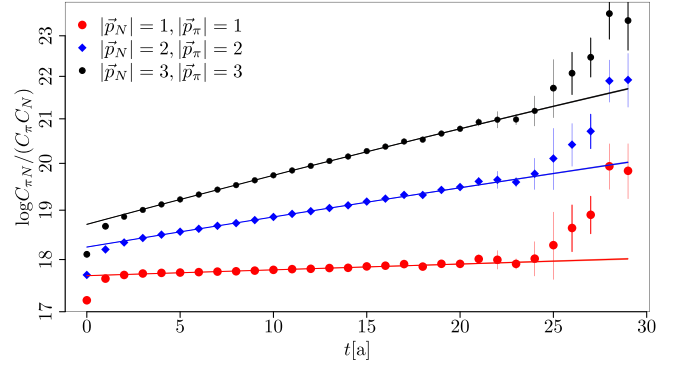


FIG. 4. The correlation function C^R for the ground state in the H_g irrep, center-of-mass frame with zero total momentum and with each hadron carrying 1 (red circles), 2 (blue circles), or 3 (black circles) units of back-to-back momentum. The solid lines show linear fits with the values of the energy gap $\Delta E_{|\vec{p}_N|=1} = -0.0113(9)$, $\Delta E_{|\vec{p}_N|=2} = -0.0612(9)$, $\Delta E_{|\vec{p}_N|=3} = -0.103(9)$ and χ^2 per degrees of freedom $\chi^2_{|\vec{p}_N|=1} = 0.53$, $\chi^2_{|\vec{p}_N|=2} = 0.52$, $\chi^2_{|\vec{p}_N|=3} = 0.4$, respectively.

energy shift and interacting energy level is part of our systematic error analysis.

5. Correlation matrix basis selection

For our analysis, we progressively add interpolating fields to the correlation matrix used, selecting the most appropriate basis by checking the stability of the spectrum. In particular, the steps we follow are

- (1) We include all the relevant single-nucleon and pion momentum combinations and occurrences and perform a GEVP analysis.
- (2) Based on the eigenvectors obtained from the full GEVP analysis, we restrict the GEVP to using the interpolating operators that dominate the first few energy levels.
- (3) Starting from the smaller GEVP of the previous step, we gradually extend the basis. The interpolating operators to be added are chosen by observing the effective mass of their diagonal correlators, and whether they yield higher-energy states than already seen in the smaller GEVP. As we add these interpolating operators, we check that the statistical errors of the lower-lying energy spectrum do not deteriorate.

In Fig. 5, we illustrate the basis selection process using an example taken from the GEVP method and the center-of-mass frame irrep H_g . What is plotted are the five components of each eigenvectors obtained via the GEVP, which is solved on each time slice. These correspond to the overlaps of each interpolating field used with the lowest-lying energy state. For a certain choice of eigenvector v^n obtained via the GEVP, and interpolating operator number α , the overlap is defined as

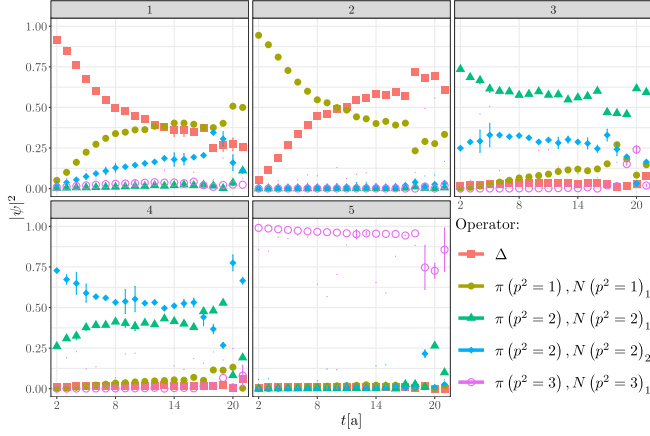


FIG. 5. The components of the first five eigenvectors obtained from a GEVP in the centre-of-mass frame irrep H_g . The number in the title of each figure corresponds to n in Eq. (26), while the different symbols denote the interpolating operator $[O_\alpha$ in Eq. (26)] as indicated in the legend.

$$|\psi|^2 = |v_\alpha^n|^2 = |\langle n|O_\alpha^\dagger|0\rangle|^2. \quad (26)$$

The eigenvectors are normalized to unity, $\sum_\alpha |v_\alpha^n|^2 = 1$ for all n . From Fig. 5, we see that the first two eigenvectors of the GEVP are largely dominated by the amplitudes from two interpolators, $O_\Delta^{H_g}$ and $O_{N\pi}^{H_g}(\vec{p}, -\vec{p})$ with $\vec{p}^2 = 1$.

We note that this same basis was used for Fig. 2 discussed earlier, where we see that the pion-nucleon interpolating field decreases the ground-state energy in the particular channel we consider here. We use this basis to extract energy levels for the analysis that follows.

B. Lattice spectrum and stability test

The four methods detailed above are complementary in the way the excited state contamination is treated. Thus, by comparing the results obtained among them, we can check the robustness of our observed energy levels. The comparison is carried out for all irreps considered, observing the stability of the results as we increase the initial fit range (t_{\min}). An example is shown in Fig. 6, where the four methods are compared for the specific case of the H_g irrep. As can be seen in this plot, the PGEVM and ratio methods provide stable results at smaller t_{\min} compared to the standard GEVP. Furthermore, the statistical errors carried by the ratio method confirm our expectation that the correlations between numerator and denominator in Eq. (22) help in reducing the statistical fluctuations in the energy shift from the noninteracting energy. This same analysis is carried out for all irreps, with the corresponding plots given in Appendix A. By observing the stability of the fitted masses as t_{\min} is increased, as well as the $\chi^2/\text{d.o.f.}$ of the fit, we indicate our selected values for each level and for

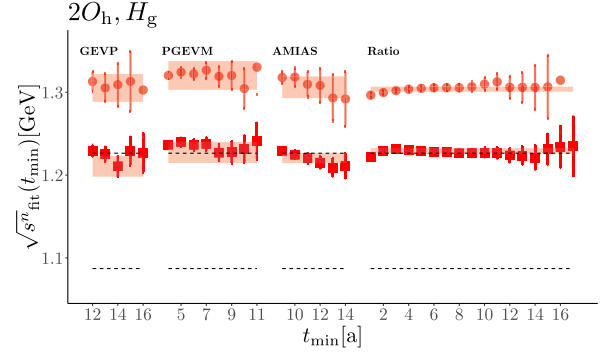


FIG. 6. Energy levels for the case of the H_g irrep. The set of points, from left to right, correspond to results from the GEVP method, the PGEVM method, AMIAS, and the ratio method. Dashed lines indicate noninteracting levels for comparison. The red bands correspond to values listed in Table VIII for GEVP, PGEVM, and AMIAS, and to the values with the smallest t_{\min} listed in Table IX for the ratio method.

each method with the bands and in Appendix B collect the results for GEVP, PGEVM, and AMIAS in Table VIII and for the ratio method in Table IX, where we also include results for two larger t_{\min} values that we use in a model averaging for our final result in Sec. VA.

In Fig. 7, we collect all the energy levels extracted from all irreps considered, using all four methods. The πN threshold ($E_{2-\text{thr}}$) and $\pi\pi N$ ($E_{3-\text{thr}}$) are shown for comparison at 1080 MeV and 1220 MeV respectively. Furthermore, for each irrep we indicate the permitted noninteracting energy levels that correspond to the lattice volume of the ensemble used. For GEVP and PGEVM, the band, indicating the uncertainty of the energy levels, contains both statistical and a systematic error from the fit-range variation. For AMIAS the systematic error from varying the fit range is negligible. For the ratio method we include only statistical errors here. A dedicated discussion of how we obtain the systematic errors of the ratio method is given in Sec. VA.

As can be seen, the GEVP, PGEVM, and AMIAS methods yield comparable statistical errors, while the ratio method yields smaller statistical errors, as expected given the previous discussion of Fig. 6. In general, we can identify several energy levels that are incompatible with noninteracting energy levels, however the statistical errors carried by our results, combined with the proximity of the $\pi\pi N$ threshold and the first noninteracting energy, make clearly identifying the Δ resonance rather challenging, even with the large statistics of $\mathcal{O}(10^4)$ used in this work. Our analysis, when compared to the analogous mesonic system of the ρ resonance [52], highlights the increased requirements for extracting resonance parameters of systems that include baryons and when using physical point ensembles.

All data plotted in Fig. 7 are included in Tables VIII and IX of Appendix B.

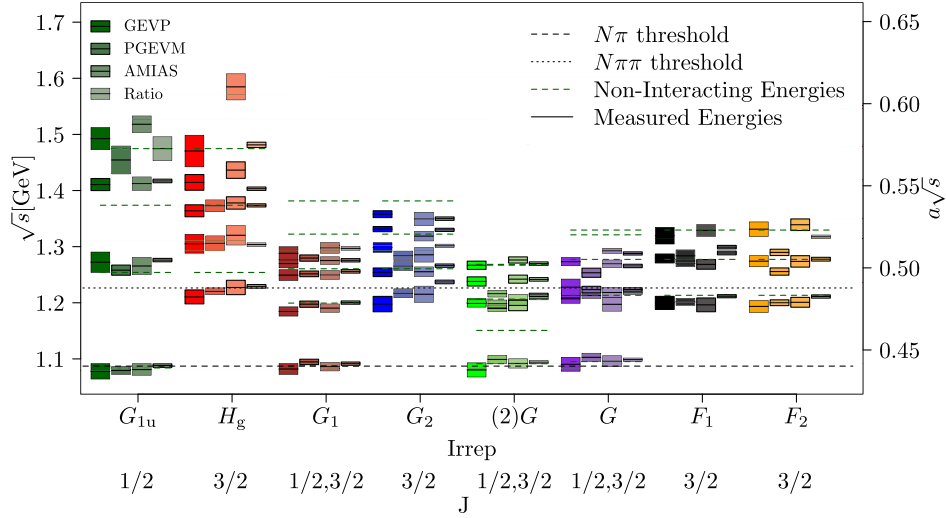


FIG. 7. The πN interacting two-hadron energy levels obtained by our analysis. For each irrep and total angular momentum J , indicated on the x -axis, we include results using the four methods employed, namely, from left to right, the GEVP method, the PGEVM method, AMIAS, and the ratio method, with the band height indicating our estimated uncertainties as explained in the text. On the left y -axis we indicate the energy levels in physical units, while on the right y -axis in lattice units. The gray dashed and dotted lines spanning the entire x -axis correspond to the πN and $\pi\pi N$ thresholds, namely 1080 MeV and 1220 MeV, respectively. The green, thicker dashed lines correspond to the noninteracting πN energy levels permitted for each irrep and for the volume used in this work.

V. SCATTERING PARAMETERS

The scattering amplitude near the resonance is well described by a Breit-Wigner type resonance. We thus parametrize the Δ -resonance phase shift, which via the Lüscher quantization condition then predicts the finite-volume energy spectrum. The lattice spectrum we have determined is then fitted to the prediction, and from the minimization of χ^2 we extract the optimal parameters of the resonance given our spectrum results. In practice, we determine the roots of the quantization condition of Eq. (1) for the given set of resonance parameters and construct a correlated, nonlinear χ^2 , given by

$$\chi^2 = \sum_{i \in (\Gamma, n)} \sum_{j \in (\Gamma, n)} \xi_i w_{ij}^{-1} \xi_j, \quad (27)$$

$$\xi_i = aE_{\text{cms}}^{i, \text{lat}} - aE_{\text{cms}}^i(L, M_R, \Gamma_R, a_0),$$

where w_{ij} is the covariance matrix between the lattice data for $aE_{\text{cms}}^{i, \text{lat}}$ and $aE_{\text{cms}}^{j, \text{lat}}$ estimated using jackknife resampling. To determine the errors of the fit parameters via the jackknife procedure, we perform the minimization of χ^2 in each jackknife sample. In Table V, we collect the results obtained for the scattering parameters when using the energy levels determined via the GEVP, PGEVM, or AMIAS methods. For the ratio method, which we will use to quote our final values, we carry out a more thorough analysis of the errors that we describe later in this manuscript. For the results in Table V, we either restrict to using only P -wave dominated irreps, with partial wave $J = 3/2$ and $\ell = 1$, which involves including five levels in the χ^2

minimization, or we use S - and P -wave dominated irreps, with two partial waves $(J, \ell) = (3/2, 1)$ or $(1/2, 0)$, thus including in total 14 energy levels. For the latter case, we estimate the scattering length from the combined S - and P -wave fits via Eqs. (2) and (3). In this work we restrict to providing the scattering length only for this channel, leaving the isospin-1/2 case for a future publication.

As can be seen from Table V, results when using the three methods are overall compatible and within statistical errors are consistent with the experimental determinations of the Δ mass and width. However, the statistical errors for the resonance width are large and do not permit a

TABLE V. Results for the scattering parameters, namely the resonance mass, M_R , resonance width, Γ_R , and scattering length, $M_\pi a_0$, using the Lüscher quantization condition and energy levels determined via the GEVP, PGEVM, and AMIAS methods. First three rows when using P -wave only and last three rows when using $S - P$ wave dominant irreps.

Method	Breit-Wigner parameters			
	M_R [MeV]	Γ_R [MeV]	$M_\pi a_0$	$\chi^2/\text{d.o.f.}$
Fit to $(J, \ell) = (3/2, 1)$; No. of \sqrt{s} points = 5				
GEVP	1249(42)	180(240)	...	0.61
PGEVM	1274(63)	160(260)	...	0.55
AMIAS	1271(40)	160(260)	...	0.47
Fit to $(J, \ell) = (1/2, 0)$ and $(3/2, 1)$; No. of \sqrt{s} points = 14				
GEVP	1262(36)	190(135)	-0.20(7)	0.82
PGEVM	1270(36)	142(207)	-0.04(24)	0.29
AMIAS	1274(11)	180(180)	-0.20(14)	1.28

significant comparison with experiment. We, therefore, opt to using the ratio method, presented below, to quote our final results for the resonance parameters. We note that for the results in Table V, an interpolation method was used to accelerate the minimization of χ^2 in each jackknife bin, described in detail in Appendix C.

A. Results using the ratio method

The most accurately determined energy levels are obtained using the ratio method and are employed to obtain our final values of the resonance parameters. Given these smaller errors, a thorough analysis of the sources of systematic errors is merited, and we, therefore, consider the following in our fits when using the ratio method:

- (1) We consider two different ranges of center-of-mass energies, namely (a) including only energy levels below $N\pi\pi$ threshold ($E_{3\text{-thr}}$), which leads to including 12 energy levels, and (b) energy levels up to $\Delta\pi$ ($E'_{3\text{-thr}}$), which leads to including 14 levels. The latter is defined by the onset of the rise of the inelasticity in the $J = 3/2$, $\ell = 1$ pion nucleon scattering channel [38].
- (2) We explore the partial wave dependence, i.e. we consider fits with energy levels coming only from P -wave dominant irreps, which leads to including five levels, and energy levels having also an S -wave contribution, which leads to the combinations mentioned in the previous item. We attempted to include higher partial waves but this led to prohibitively large statistical errors on the parameters.
- (3) The S -wave contribution is entirely parametrized by the scattering length, which can be obtained directly from the ratio of correlators used in the ratio method, as presented in more detail in Sec. VB below. We either perform fits using this direct determination of the scattering length or leaving the scattering length free as an additional fit parameter.
- (4) We use three different fit ranges for the energy levels, i.e. three values of t_{\min} , that indicatively span between $t_{\min} \simeq 0.3$ fm and 1 fm. The smallest t_{\min} is determined from the onset of the plateau in the ratio method and is that corresponding to the band in Figs. 6, 11–18. The largest t_{\min} is determined from the onset of the plateau in the single exponential fit to the principal correlator from the GEVP. An intermediate t_{\min} is also used between these two values.
- (5) We vary the noninteracting energy level, i.e. that of the denominator in Eqs. (22) and (23) in the ratio method. We found in our fits, that the energy levels most sensitive to this variation are the ones for the H_g irrep. We, therefore, perform a separate analysis for the H_g energy levels using the ratio method with pion-nucleon states with three values of back-to-back momenta, namely $\vec{p}_N^2 = \vec{p}_\pi^2 = (\frac{2\pi}{L})^2 \cdot \{1, 2, 3\}$, as in Fig. 4.

Considering these variations, our analysis yields 45 results, over which we quantify our systematic uncertainty. The results are tabulated in Table X of Appendix D.

The results of the different fits are model averaged according to Ref. [53] to derive a combined statistical and systematic error. As an example, in Fig. 8, we show our result for the P -wave phase shift for one of the 45 fits that has a significant contribution to the model average.

The cumulative distribution function (CDF) for the resonance parameters obtained from the 45 different fits is shown in Fig. 9. Our final result for the resonance mass and width obtained through model averaging are

$$M_R = 1269(39)_{\text{Stat}}(45)_{\text{Total}} \text{ MeV},$$

$$\Gamma_R = 144(169)_{\text{Stat}}(181)_{\text{Total}} \text{ MeV},$$

respectively, where the first error is the statistical error and the second is the total, combining statistical and systematic errors. For the individual contributions of the different sources of systematic error, we refer to Table VI. The systematic error for each source of uncertainty (a) is estimated via

$$\sigma_{\text{sys}}^a = \sqrt{\sum_{i=1}^{N_a} \mathcal{O}_i^2 p_i - \left(\sum_{i=1}^{N_a} \mathcal{O}_i p_i\right)^2}, \quad (28)$$

where \mathcal{O}_i and p_i are averaged over all other systematics other than a and N_a is the number of variations for the given systematic error.

For the $I = 3/2$ S -wave scattering length, we obtain from the combined S - and P -wave fit of the lattice spectrum

$$M_\pi a_0 = -0.16(11).$$

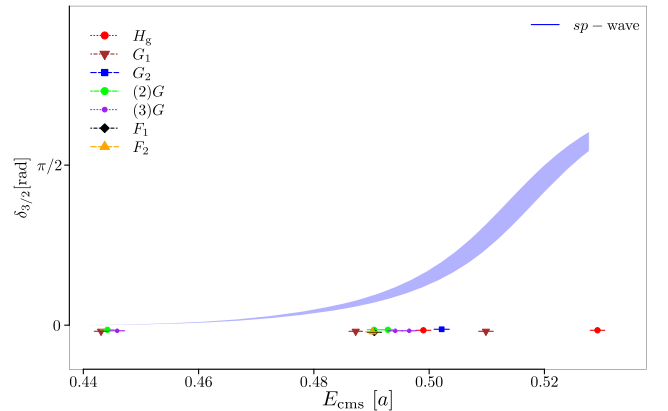


FIG. 8. The P -wave phase-shift as a function of the invariant mass $E_{\text{cms}} = \sqrt{s}$. The error band is determined using jackknife resampling. The points with horizontal error bars show each fitted energy level included its jackknife error bar.

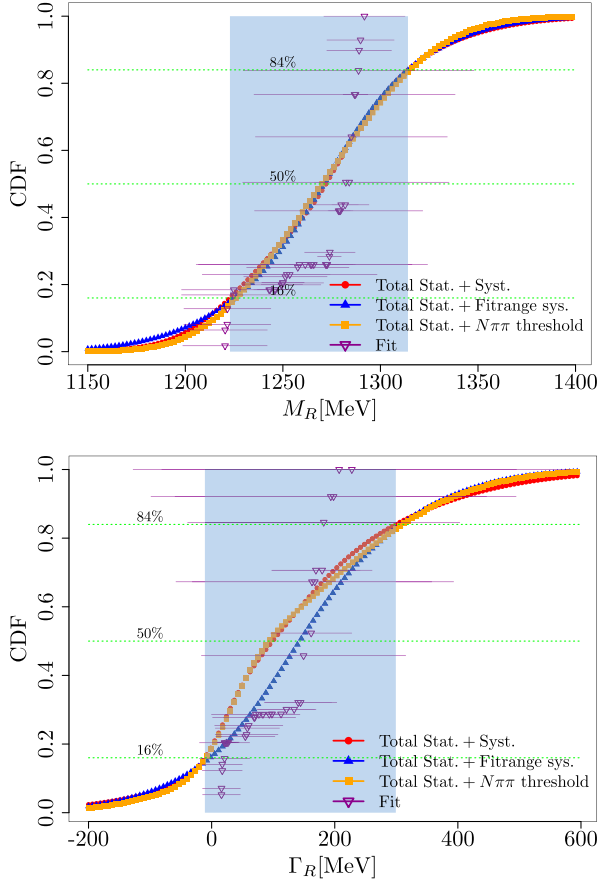


FIG. 9. The cumulative probability distribution function for the model averaging carried out to obtain the resonance mass M_R (top) and the resonance width Γ_R (bottom). We distinguish between systematics arising from the energy-level fit range choice (blue triangles), considering energy levels also slightly above $N\pi\pi$ threshold (brown squares) and including all five sources of systematic errors as explained in the text (red small circles). For the resonance mass all three curves fall on top of each other, while for the width the yellow squares are on top of the red circles. Each dark magenta point corresponds to the central value and statistical error of one particular fit with y -axis corresponding to the numerically determined CDF. The vertical band shows the range of M_R (top) and Γ_R (bottom) between 16% and 84% which we take as our total error.

For further illustration, in Fig. 9, we show separately the systematics that originate from varying the fit ranges, from using different noninteracting levels in the ratio method and considering the two center-of-mass energy ranges. The fact that these curves collapse onto the curve that corresponds to the total statistical plus systematic error indicates that our dominant source of error is statistical.

B. Direct extraction of the scattering length

The scattering amplitude in the S -wave around the πN threshold can be well-described by the leading-order effective range expansion using a single parameter, the

TABLE VI. Individual contributions to the total systematic uncertainty, obtained as explained in the text. Enumeration of the source of systematic uncertainty (a) follows that of Sec. VA.

Criterion (a)	N_a	ΔM_R [MeV]	$\Delta \Gamma_R$ [MeV]
Inclusion of energies above $N\pi\pi$ (1)	2	35	63
P - or P - and S -wave (2)	2	1	1
Fit or fixed scattering length (3)	2	26	10
Fit range (4)	3	2	7
Momenta in H_g (5)	3	4	6

scattering length. As an alternative to the analysis of the previous section, by which the scattering length is extracted from the phase shift, we can extract this quantity from the energy shift ΔE obtained directly from the ratio method. In particular, correlation functions computed with increased statistics, indicated in the first row of Table IV, allow for a high-statistics calculation of the levels in the G_{1u} irrep. Using the first level of this irrep and the effective range expansion, we determine the scattering length from [1]

$$\Delta E \cdot L = -\frac{2\pi}{\mu_{\pi N} L} \frac{a_0}{L} \left(1 + c_1 \frac{a_0}{L} + c_2 \left(\frac{a_0}{L} \right)^2 \right) + \mathcal{O}(L^{-5}). \quad (29)$$

This extraction of ΔE from the ratio method benefits from the smaller statistical errors associated with the energy shifts. The data obtained for the ratio and the resulting fit are shown in Fig. 10.

For the scattering length we obtain

$$M_\pi a_0 = -0.13(4). \quad (30)$$

A comparison of our result to other work in the literature is provided in Table VII. In particular, we compare our results to a recent lattice calculation using $N_f = 2 + 1$ clover improved fermions at the heavier-than-physical pion mass of 200 MeV. We also compare to three other

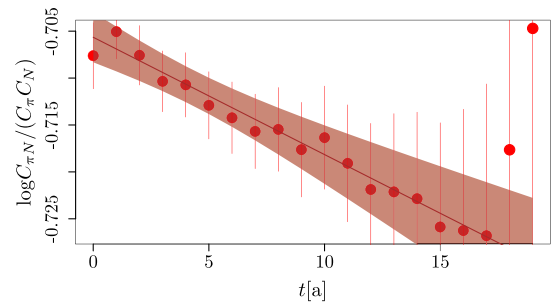


FIG. 10. The ratio method as applied to the first level of the G_{1u} irrep. With red band we indicate our fit in the range $\frac{t}{a} \in [3, 17]$.

TABLE VII. Scattering length in the isospin-3/2 pion-nucleon channel. We compare our result, obtained via Eq. (29), to a lattice calculation using 200 MeV pion mass [6], a calculation using pionic atom data [58], a calculation using unitarized ChPT [59], and a phenomenological determination via global fits to pion-nucleon cross-section data [60]. The error in our determination is only statistical.

	M_π (MeV)	$M_\pi a_0^{3/2}$
This work	139	-0.13(4)
Bulava <i>et al.</i> [6]	200	-0.2735(81)
Pionic atoms [58]	140	-0.0865(18)
Unitarized ChPT [59]	140	-0.0894(17)
Phenomenology [60]	140	-0.0867(35)

determinations, namely from pionic atoms [54–57] using the values of the scattering lengths updated in Ref. [58], from unitarized chiral perturbation theory [59], and from a global fit to low-energy pion-nucleon cross-section data [60]. Within our quoted statistical uncertainty, our result is consistent with the latter three results.

VI. CONCLUSIONS

Using an ensemble of twisted mass fermions simulated with two degenerate light quarks, and strange and charm quarks with masses tuned to their physical values, we determine the Breit-Wigner resonance parameters of the lowest lying resonance in the $\pi N I(J^P) = \frac{3}{2}(\frac{3}{2}^+)$ channel. To our knowledge, this is the first such lattice study using physical point simulations. We use a large number of measurements in order to tackle the expected increase of the statistical uncertainties in the meson-baryon correlation functions. To determine the energy levels, we form correlation matrices of one and two-particle correlation functions after an appropriate group-theoretic projection to the relevant lattice irreducible representations. We employ four methods to extract the energy levels from the correlation functions, including the standard GEVP method and variants thereof. While the four methods yield consistent results, the ratio method, where we determine the energy gap between interacting and noninteracting energy levels via appropriate ratios of two-hadron to single-hadron correlation functions, yields considerably smaller statistical errors.

Restricting our analysis to energy levels obtained via the ratio method, we solve the Lüscher quantization condition to extract the resonance mass and width, varying our fits to probe systematic uncertainties. For the scattering length, we use a direct approach, forming a ratio between correlation functions with increased statistics to obtain the energy shift between noninteracting and interacting states explicitly. For the resonance parameters we find the values,

$$\begin{aligned}
 M_\pi a_0 &= -0.13(4), \\
 M_R &= 1269(45) \text{ MeV}, \quad \text{and} \\
 \Gamma_R &= 144(181) \text{ MeV},
 \end{aligned}
 \tag{31}$$

for the scattering length in the 3/2 isospin channel, the resonance mass, and the resonance width, respectively. Our result for the scattering length compares well with phenomenological determinations [61] and determinations from chiral perturbation theory (ChPT) [5,58–60]. A recent lattice study using simulations with 200 MeV pions [6] yields a value between 1.4 and 2.7 times larger than our value when taking into account our statistical uncertainties, a factor which is compatible with the ratio of pion masses used. Our result for the resonance mass is compatible with the expected 1230–1234 MeV values quoted by the PDG [62], while our value for the resonance width has large uncertainties, requiring more lattice input to be determined with significance. As a first application of the Lüscher method to the $\pi N - \Delta$ channel at the physical point, this calculation was restricted to a single ensemble, which does not allow for a complete assessment of lattice systematic errors, such as cutoff effects. The current study, and in particular the level of precision obtained given the statistics used, paves the way for future calculations with multiple physical point ensembles allowing for controlled continuum and infinite volume extrapolations.

ACKNOWLEDGMENTS

F. P. acknowledges financial support by the Cyprus Research and Innovation Foundation under contracts with numbers EXCELLENCE/0918/0129 and EXCELLENCE/0421/0195. C. A. acknowledges support by the Cyprus Research and Innovation foundation under contract with number EXCELLENCE/0421/0043. M. P. acknowledges support by the Sino-German collaborative research center CRC 110. This work was supported by a grant from the Swiss National Supercomputing Centre (CSCS) under projects with IDs s702, s954, and s1174. We also acknowledge PRACE for awarding us access to Piz Daint, hosted in Switzerland. The authors gratefully acknowledge the Gauss Centre for Supercomputing e.V. ([63]) for funding this project by providing computing time through the John von Neumann Institute for Computing (NIC) on the GCS Supercomputer JUWELS-Booster [64] at Jülich Supercomputing Centre (JSC).

APPENDIX A: PLOTS COMPARING GEVP, PGEVM, AMIAS, AND THE RATIO METHOD

In Figs. 11–18 we plot the extracted energy levels in all irreps for all four methods as a function of the lower fit range. The figures follow the conventions of Fig. 6 in the main text.

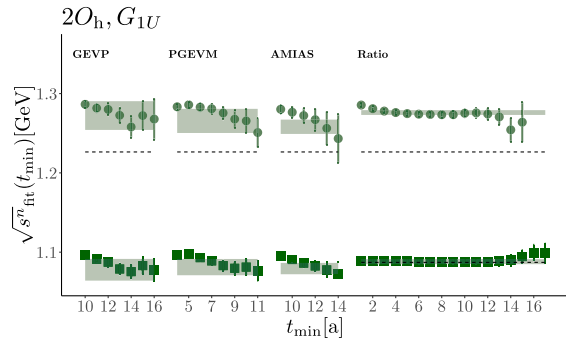


FIG. 11. $N\pi$ energy level fits using the GEVP, PGEVM, AMIAS, and Ratio methods for the irrep G_{1U} . The colored bands correspond to our final selection that is used in Fig. 7.

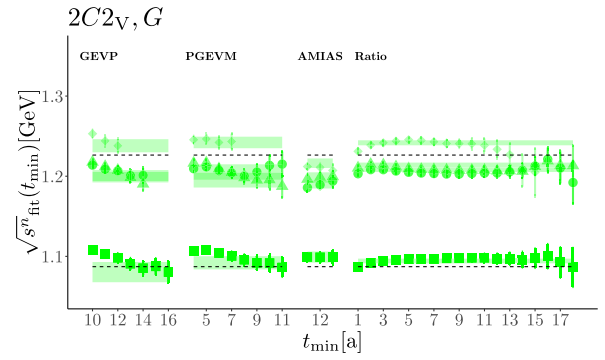


FIG. 15. Same as in Fig. 11 but for irrep $2G$.

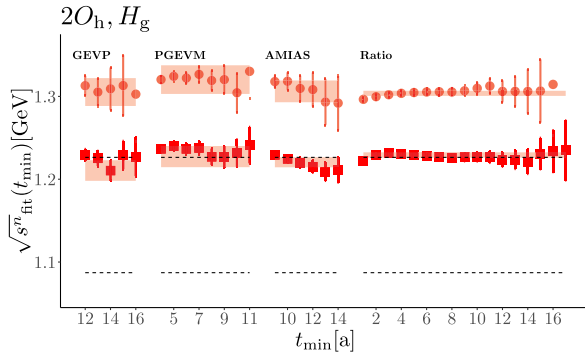


FIG. 12. Same as in Fig. 11 but for irrep H_g .

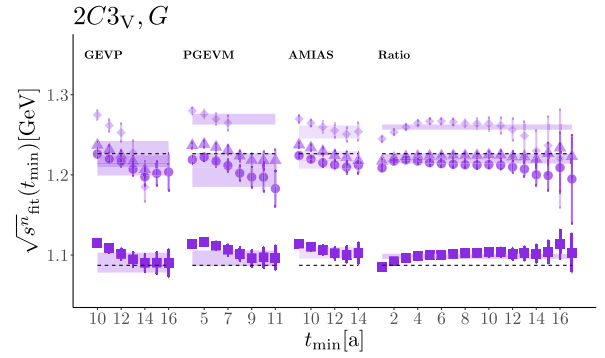


FIG. 16. Same as in Fig. 11 but for irrep $3G$.

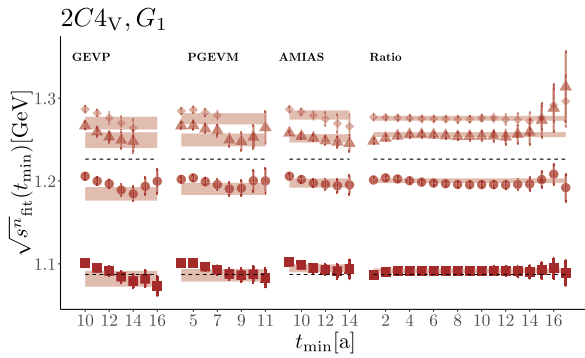


FIG. 13. Same as in Fig. 11 but for irrep G_1 .

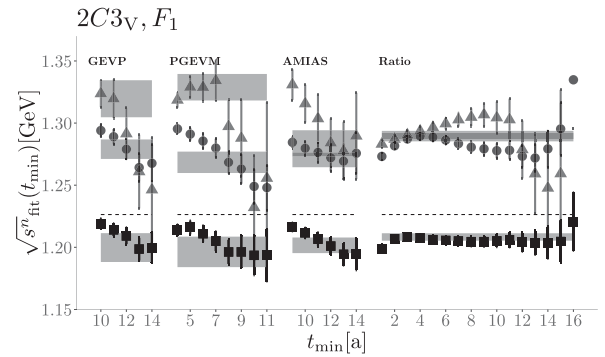


FIG. 17. Same as in Fig. 11 but for irrep F_1 .

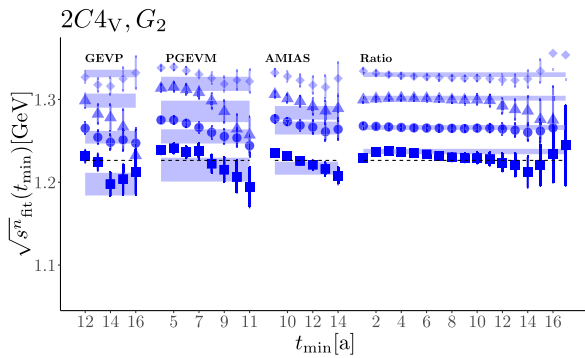


FIG. 14. Same as in Fig. 11 but for irrep G_2 .

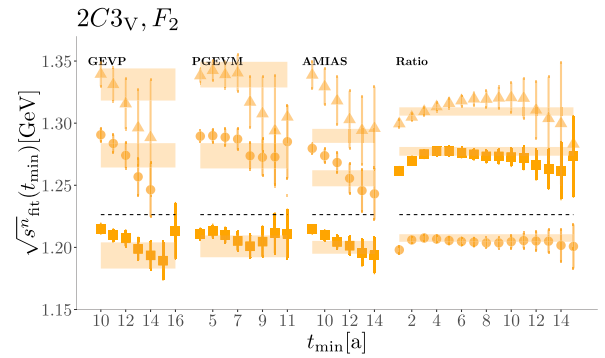


FIG. 18. Same as in Fig. 11 but for irrep F_2 .

APPENDIX B: SPECTRUM FIT RESULTS

We list the energy levels obtained using the GEVP method, the PGEVM method, and AMIAS in Table VIII. The fit range given is the optimal one, along with the associated reduced χ^2 . For GEVP and PGEVM, the quoted uncertainty of the energy levels contains both statistical and a systematic error from the fit range variation. For AMIAS

the systematic error from varying the fit range is negligible. For the ratio method, the error is purely statistical.

The ratio method energy levels that were included in Fig. 7 are listed in Table IX. The quoted uncertainty is statistical only and the closest noninteracting levels were used to obtain the energy shift. See Sec. VA and Appendix D for details on how the systematic error is

TABLE VIII. Energy levels from the $\Delta, N\pi$ correlation matrix for the three methods GEVP, PGEVM and AMIAS. We use $\vec{P} = \vec{d} \cdot 2\pi/L$. Shown are the cases $\vec{d}^2 = 0$ with group O_h^D , $\vec{d}^2 = 1$ with group C_{4v}^D , $\vec{d}^2 = 2$ with group C_{2v}^D , and $\vec{d}^2 = 3$ with C_{3v}^D . For each irrep Λ and the lowest states labeled by n we give for each method the optimal fit range ($t_{\text{range}} = [t_{\text{min}}, t_{\text{max}}]$) the associated reduced χ^2 for the fit and the energy in the center-of-mass frame in lattice units.

n	GEVP			PGEVM			AMIAS
	$t_{\text{range}} [a]$	$\frac{\chi^2}{\text{d.o.f.}}$	$a\sqrt{s_n^{\Lambda, \vec{P}}}$	$t_{\text{range}} [a]$	$\frac{\chi^2}{\text{d.o.f.}}$	$a\sqrt{s_n^{\Lambda, \vec{P}}}$	$a\sqrt{s_n^{\Lambda, \vec{P}}}$
$\vec{d}^2 = 0; \Lambda = G_{1u}$							
1	[16,23]	1.77	0.4375(55)	[10,23]	1.15	0.4388(42)	0.4381(29)
2	[15,20]	0.26	0.5164(73)	[10,20]	0.87	0.5137(61)	0.5107(36)
3	[11,17]	0.46	0.5726(43)	[7,17]	0.76	0.5732(48)	0.5904(100)
$\vec{d}^2 = 0; \Lambda = H_g$							
1	[14,23]	1.02	0.4914(50)	[9,23]	0.77	0.4982(52)	0.4954(24)
2	[13,20]	0.62	0.5298(68)	[9,20]	1.07	0.5359(70)	0.5302(53)
3	[13,21]	1.52	0.5536(43)	[9,21]	1.57	0.5593(44)	0.5572(43)
$\vec{d}^2 = 1; \Lambda = G_1$							
1	[15,24]	2.47	0.4392(38)	[9,24]	1.85	0.4409(30)	0.4443(19)
2	[14,22]	2.50	0.4808(33)	[8,22]	2.15	0.4832(29)	0.4860(22)
3	[13,22]	1.08	0.5071(38)	[8,22]	0.79	0.5072(31)	0.5080(20)
4	[13,23]	0.66	0.5155(31)	[8,23]	0.57	0.5176(27)	0.5194(22)
$\vec{d}^2 = 1; \Lambda = G_2$							
1	[14,24]	1.19	0.4861(55)	[9,24]	1.30	0.4932(58)	0.4940(32)
2	[13,26]	1.57	0.5092(31)	[9,26]	1.71	0.5095(34)	0.5136(32)
3	[12,25]	0.99	0.5271(34)	[9,25]	0.79	0.5218(52)	0.5211(33)
$\vec{d}^2 = 2; \Lambda = G$							
1	[16,28]	1.91	0.4385(51)	[9,28]	1.34	0.4432(33)	0.4461(28)
2	[13,19]	1.85	0.4874(28)	[9,18]	1.60	0.4851(38)	0.4925(22)
3	[13,26]	2.48	0.4866(26)	[9,25]	1.99	0.4892(39)	0.4966(24)
4	[13,25]	2.08	0.5025(33)	[6,25]	1.78	0.5042(29)	0.5088(33)
$\vec{d}^2 = 3; \Lambda = G$							
1	[15,24]	2.13	0.4426(50)	[9,24]	1.27	0.4448(39)	0.4476(29)
2	[13,21]	0.79	0.4899(32)	[9,21]	0.62	0.4860(49)	0.4924(22)
3	[13,22]	1.93	0.4940(30)	[9,22]	1.41	0.4945(35)	0.4966(24)
4	[13,23]	2.86	0.4983(58)	[6,23]	2.34	0.5153(27)	0.5088(33)
$\vec{d}^2 = 3; \Lambda = F_1$							
1	[14,19]	0.91	0.4849(44)	[9,19]	0.67	0.4857(50)	0.4878(25)
2	[12,19]	1.00	0.5195(32)	[8,18]	1.32	0.5148(34)	0.5157(24)
3	[11,19]	1.07	0.5366(63)	[6,19]	1.11	0.5394(43)	0.5210(43)
$\vec{d}^2 = 3; \Lambda = F_3$							
1	[14,22]	1.60	0.4844(42)	[8,22]	1.37	0.4874(35)	0.4871(21)
2	[12,18]	1.98	0.5172(40)	[8,18]	1.21	0.5170(41)	0.5096(26)
3	[11,19]	0.53	0.5403(52)	[6,19]	0.45	0.5435(42)	0.5235(22)

TABLE IX. Energy levels in lattice units from the Δ , $N\pi$ correlation matrix obtained using the ratio method for all kinematic frames and for multiple fit ranges (using the same t_{\max}). The first t_{\min} corresponds to the one shown in Fig. 7, the last one equals the optimal fit range for the corresponding GEVP correlator and the middle one is halfway between the previous two. We used the closest noninteracting level in the ratio denominator Eq. (22). Errors are statistical only.

n	$t_{\text{range}} (\{t_{\min}, \}; t_{\max})[a]$		$\frac{\chi^2}{\text{d.o.f.}}(\{t_{\min}, \}), a\sqrt{s_n^{\Lambda, \vec{P}}}(\{t_{\min}, \})$				
$\vec{d}^2 = 0; \Lambda = G_{1u}$							
1	[7,10,14;22]	0.34	0.4416(13)	0.39	0.4416(16)	0.55	0.4424(27)
2	[4,8,13;17]	0.63	0.5180(12)	0.33	0.5169(15)	0.58	0.5158(42)
3	[3,7,12;15]	3.61	0.5752(13)	0.30	0.5707(19)	0.32	0.5702(64)
$\vec{d}^2 = 0; \Lambda = H_g$							
1	[5,9,14;23]	0.52	0.4990(13)	0.43	0.4978(20)	0.60	0.4957(60)
2	[4,9,13;18]	0.48	0.5292(12)	0.52	0.5304(24)	0.54	0.5302(74)
3	[3,8,13;17]	1.69	0.5576(11)	0.52	0.5550(15)	0.58	0.5498(47)
4	[3,7,12;17]	0.62	0.5696(12)	0.79	0.5695(17)	0.30	0.5698(59)
5	[4,7,11;14]	0.91	0.6013(19)	0.79	0.5695(17)	0.30	0.5689(59)
$\vec{d}^2 = 1; \Lambda = G_1$							
1	[4,10,15;23]	0.10	0.4431(12)	0.11	0.4432(17)	0.13	0.4434(41)
2	[4,10,14;23]	1.67	0.4873(12)	0.58	0.4854(16)	0.85	0.4856(31)
3	[4,10,13;20]	0.44	0.5098(13)	0.55	0.5091(23)	0.76	0.5100(46)
4	[4,10,13;20]	0.35	0.5178(12)	0.43	0.5179(18)	0.56	0.5172(32)
5	[5,8,13;20]	0.41	0.5265(13)	0.47	0.5270(18)	0.63	0.5285(57)
$\vec{d}^2 = 1; \Lambda = G_2$							
1	[4,8,14;23]	1.06	0.5022(13)	0.42	0.4993(19)	0.41	0.4920(76)
2	[4,8,13;23]	0.31	0.5140(12)	0.33	0.5135(15)	0.46	0.5126(32)
3	[3,7,12;18]	0.35	0.5283(12)	0.41	0.5279(15)	0.37	0.5246(38)
4	[3,7,11;21]	1.07	0.5398(11)	0.46	0.5385(13)	0.58	0.5379(19)
5	[3,7,11;18]	0.30	0.5479(12)	0.31	0.5475(16)	0.39	0.5488(30)
$\vec{d}^2 = 2; \Lambda = G$							
1	[3,10,16;24]	0.81	0.4442(12)	0.16	0.4458(19)	0.22	0.4466(62)
2	[3,7,13;21]	2.02	0.4904(12)	0.39	0.4885(13)	0.56	0.4894(29)
3	[3,7,13;22]	3.44	0.4928(12)	0.26	0.4905(13)	0.37	0.4899(23)
4	[3,6,12;17]	1.53	0.5040(12)	0.58	0.5052(15)	0.49	0.5007(44)
5	[3,6,11;17]	1.52	0.5154(12)	0.66	0.5157(14)	0.41	0.5127(28)
$\vec{d}^2 = 3; \Lambda = G$							
1	[4,10,15;21]	0.61	0.4460(12)	0.17	0.4480(20)	0.25	0.4481(58)
2	[4,10,15;21]	1.10	0.4941(13)	0.24	0.4923(20)	0.14	0.4867(76)
3	[4,8,13;23]	0.24	0.4965(12)	0.28	0.4968(15)	0.34	0.4963(32)
4	[3,8,13;18]	3.75	0.5113(13)	0.30	0.5131(22)	0.34	0.5069(74)
5	[3,8,13;18]	0.12	0.5213(12)	0.13	0.5213(15)	0.05	0.5192(30)
$\vec{d}^2 = 3; \Lambda = F_1$							
1	[3,10,14;20]	0.65	0.4905(12)	0.27	0.4892(20)	0.40	0.4886(52)
2	[5,9,12;18]	1.54	0.5231(14)	0.49	0.5198(18)	0.54	0.5169(37)
3	[3,7,11;17]	2.06	0.5238(13)	0.55	0.5288(23)	0.80	0.5288(69)
$\vec{d}^2 = 3; \Lambda = F_2$							
1	[3,10,14;19]	0.72	0.4902(12)	0.34	0.4890(21)	0.60	0.4878(52)
2	[5,8,12;19]	0.46	0.5184(14)	0.27	0.5167(20)	0.30	0.5140(49)
3	[3,7,11;17]	1.68	0.5315(14)	0.11	0.5356(22)	0.17	0.5354(69)

computed for the ratio method, which we quote in our final results.

APPENDIX C: OPTIMIZATION OF QUANTIZATION CONDITION SOLUTION

As explained in the text, the statistical errors quoted for the resonance parameters are obtained via jackknife resampling. To determine these, we perform the minimization of χ^2 in each jackknife sample, which in turn requires evaluating the so-called zeta function and finding the roots of the quantization condition in every iteration of the χ^2 minimization algorithm for every jackknife sample. While this is carried out explicitly for our final results that use the ratio method, for the fits to the spectrum results using the GEVP, PGEVM, and AMIAS methods shown in Table V, we accelerate this process by employing a multidimensional spline interpolation in the parameters being fitted and evaluate the quantization condition at the grid points of this interpolation. The spline interpolation function is uniquely defined by the values of each finite volume energy level at each grid point $E^{\vec{P},\Lambda}(M_{R,l}, \Lambda_{R,m}, a_{0,n})$ with $l = 0, \dots, L-1$, $m = 0, \dots, M-1$, and $n = 0, \dots, N-1$. We determine our grid by first carrying out trial fits of our data, obtaining the errors of the fit parameters via their covariance matrix. From these initial fits, we found that the following grid contains the parameters.

$$\begin{aligned} M_{R,i} &\in [1100, 1500] \text{ MeV}, \\ \Gamma_{R,j} &\in [50, 300] \text{ MeV}, \\ a_{0,k} &\in [-0.0025, -0.0001] \text{ MeV}^{-1}. \end{aligned} \quad (\text{C1})$$

The number of points in each dimension is taken as $L = 50$, $M = 50$, and $N = 8$, which we ascertain is fine

enough to reproduce all our trial fit results. The definition of our spline interpolation function can be written as

$$S(M_R, \Gamma_R, a_0) = \sum_{i=0}^3 \sum_{j=0}^3 \sum_{k=0}^3 C_{l,m,n}^{i,j,k} t_l^i u_m^j r_n^k, \quad (\text{C2})$$

where $(M_R, \Gamma_R, a_0) \in [M_{R,l}, M_{R,l+1}] \times [\Gamma_{R,n}, \Gamma_{R,n+1}] \times [a_{0,l}, a_{0,l+1}]$, and t , u , r are the following dimensionless coefficients:

$$\begin{aligned} t_l &= \frac{M_R - M_{R,l}}{\Delta M_{R,l}}, \\ u_m &= \frac{\Gamma_R - \Gamma_{R,m}}{\Delta \Gamma_{R,m}}, \\ r_n &= \frac{a_0 - a_{0,n}}{\Delta a_{0,n}}, \end{aligned} \quad (\text{C3})$$

with the corresponding widths

$$\begin{aligned} \Delta M_{R,l} &= M_{R,l+1} - M_{R,l}, \\ \Delta \Gamma_{R,m} &= \Gamma_{R,m+1} - \Gamma_{R,m}, \\ \Delta a_{0,n} &= a_{0,n+1} - a_{0,n}. \end{aligned} \quad (\text{C4})$$

The spline coefficients C in Eq. (C2) are determined using the algorithm detailed in Ref. [65].

APPENDIX D: SYSTEMATIC UNCERTAINTIES IN THE RATIO METHOD

For our final results for the resonance mass and resonance width, we use the results from the ratio method and obtain a systematic by varying the fit to the Lüscher quantization as described in Sec. VA. This yields 45 fits, the results of which are collected in Table X.

TABLE X. Results for the scattering parameters, namely the resonance mass, M_R , resonance width, Γ_R , and scattering length, $M_\pi a_0$, using the Lüscher quantization condition and energy levels determined from the ratio method. We delineate two of the five fit variations listed in Sec. VA via the table sub-headings, namely the variation arising from (1) varying the number of energy levels included and (2) whether considering only P - or P - and S -wave. For (3), we give the value of the scattering length a_0 when this is left as a free parameter and omit it when it is fixed via the direct evaluation. The first column labels the remaining two variations, namely (4) that obtained by varying the fit range in three ways (first index) and (5) by varying the back-to-back momenta of the noninteracting pion-nucleon operator used in the denominator of the ratio method (second index).

Fit type	Breit-Wigner parameters		$M_\pi a_0$	$\chi^2/\text{d.o.f.}$
	M_R [MeV]	Γ_R [MeV]		
	$(J, \ell) = (1/2, 0)$ and $(3/2, 1)$; No. of \sqrt{s} points = 14			
1,1	1287(7)	98(19)	-0.12(5)	1.34
1,2	1289(17)	169(72)	-0.16(7)	0.37
1,3	1291(20)	241(4)	-0.17(17)	0.21
2,1	1279(5)	83(15)	-0.12(5)	1.74
2,2	1280(14)	140(54)	-0.16(7)	0.47
2,3	1282(52)	193(250)	-0.17(17)	0.22

(Table continued)

TABLE X. (Continued)

Fit type	Breit-Wigner parameters			$\chi^2/\text{d.o.f.}$
	M_R [MeV]	Γ_R [MeV]	$M_\pi a_0$	
3,1	1272(5)	70(12)	-0.12(5)	2.18
3,2	1274(13)	121(45)	-0.16(7)	0.54
3,3	1289(60)	207(288)	-0.17(3)	0.22
1,1	1287(7)	98(19)	...	1.24
1,2	1289(16)	161(66)	...	0.40
1,3	1286(52)	182(221)	...	0.27
2,1	1279(5)	83(15)	...	1.61
2,2	1280(14)	134(40)	...	2.80
2,3	1278(43)	150(166)	...	0.28
3,1	1272(5)	70(12)	...	2.01
3,2	1274(6)	117(20)	...	0.54
3,3	1285(50)	163(195)	...	0.26
$(J, \ell) = (1/2, 0)$ and $(3/2, 1)$; No. of \sqrt{s} points = 12				
1,1	1249(10)	26(17)	-0.11(5)	0.98
1,2	1258(27)	72(72)	-0.15(7)	0.30
1,3	1221(22)	17(33)	-0.13(18)	0.14
2,1	1246(10)	23(15)	-0.11(5)	1.26
2,2	1252(23)	60(56)	-0.15(7)	0.35
2,3	1220(21)	16(30)	-0.14(19)	0.13
3,1	1243(8)	22(12)	-0.11(5)	1.60
3,2	1250(21)	57(51)	-0.15(7)	0.39
3,3	1224(26)	21(41)	-0.13(18)	0.17
1,1	1250(10)	27(17)	...	0.89
1,2	1257(26)	68(67)	...	0.28
1,3	1221(22)	17(33)	...	0.13
2,1	1246(9)	24(15)	...	1.15
2,2	1251(21)	58(52)	...	0.32
2,3	1220(22)	16(30)	...	0.12
3,1	1243(8)	22(13)	...	1.45
3,2	1249(20)	54(48)	...	0.36
3,3	1224(27)	21(40)	...	0.15
$(J, \ell) = (3/2, 1)$; No. of \sqrt{s} points = 5				
1,1	1282(7)	113(22)	...	0.77
1,2	1284(18)	180(87)	...	0.45
1,3	1265(60)	227(355)	...	0.17
2,1	1272(6)	93(16)	...	1.17
2,2	1273(14)	145(58)	...	0.45
2,3	1253(44)	167(225)	...	0.15
3,1	1264(5)	77(13)	...	1.76
3,2	1265(13)	122(48)	...	0.11
3,3	1261(54)	198(296)	...	0.20

[1] M. Luscher, *Commun. Math. Phys.* **105**, 153 (1986).[2] M. Luscher, *Nucl. Phys.* **B354**, 531 (1991).[3] M. Luscher, *Nucl. Phys.* **B364**, 237 (1991).[4] O. Bär, *Proc. Sci. LATTICE2019* (2019) 078 [arXiv:1907.03284].[5] O. Bar, *Phys. Rev. D* **101**, 034515 (2020).[6] J. Bulava, A.D. Hanlon, B. Hörz, C. Morningstar, A. Nicholson, F. Romero-López, S. Skinner, P. Vranas, and A. Walker-Loud, *Nucl. Phys.* **B987**, 116105 (2023).[7] G. Silvi *et al.*, *Phys. Rev. D* **103**, 094508 (2021).

- [8] F. Pittler, C. Alexandrou, K. Hadjiannakou, G. Koutsou, S. Paul, M. Petschlies, and A. Todaro, *Proc. Sci. LATTICE2021* (**2022**) 226
- [9] C. W. Andersen, J. Bulava, B. Hörz, and C. Morningstar, *Phys. Rev. D* **97**, 014506 (2018).
- [10] C. B. Lang, L. Leskovec, M. Padmanath, and S. Prelovsek, *Phys. Rev. D* **95**, 014510 (2017).
- [11] V. Verduci, Ph.D. thesis, Graz University, 2014.
- [12] C. B. Lang and V. Verduci, *Phys. Rev. D* **87**, 054502 (2013).
- [13] D. Mohler, *Proc. Sci. LATTICE2012* (**2012**) 003 [arXiv:1211.6163].
- [14] C. Alexandrou, J. W. Negele, M. Petschlies, A. Strelchenko, and A. Tsapalis, *Phys. Rev. D* **88**, 031501 (2013).
- [15] C. Alexandrou, J. W. Negele, M. Petschlies, A. V. Pochinsky, and S. N. Syritsyn, *Phys. Rev. D* **93**, 114515 (2016).
- [16] C. McNeile, C. Michael, and P. Pennanen (UKQCD Collaboration), *Phys. Rev. D* **65**, 094505 (2002).
- [17] C. McNeile and C. Michael (UKQCD Collaboration), *Phys. Lett. B* **556**, 177 (2003).
- [18] G. P. Engel, C. B. Lang, D. Mohler, and A. Schäfer (BGR Collaboration), *Phys. Rev. D* **87**, 074504 (2013).
- [19] J. J. Dudek and R. G. Edwards, *Phys. Rev. D* **85**, 054016 (2012).
- [20] R. G. Edwards, J. J. Dudek, D. G. Richards, and S. J. Wallace, *Phys. Rev. D* **84**, 074508 (2011).
- [21] G. P. Engel, C. B. Lang, M. Limmer, D. Mohler, and A. Schafer (BGR [Bern-Graz-Regensburg] Collaboration), *Phys. Rev. D* **82**, 034505 (2010).
- [22] C. Gattringer, C. Hagen, C. B. Lang, M. Limmer, D. Mohler, and A. Schafer, *Phys. Rev. D* **79**, 054501 (2009).
- [23] S. Basak, R. G. Edwards, G. T. Fleming, K. J. Juge, A. Lichtl, C. Morningstar, D. G. Richards, I. Sato, and S. J. Wallace, *Phys. Rev. D* **76**, 074504 (2007).
- [24] C. h. Kim, C. T. Sachrajda, and S. R. Sharpe, *Nucl. Phys.* **B727**, 218 (2005).
- [25] K. Rummukainen and S. A. Gottlieb, *Nucl. Phys.* **B450**, 397 (1995).
- [26] L. Leskovec and S. Prelovsek, *Phys. Rev. D* **85**, 114507 (2012).
- [27] C. Morningstar, J. Bulava, B. Singha, R. Brett, J. Fallica, A. Hanlon, and B. Hörz, *Nucl. Phys.* **B924**, 477 (2017).
- [28] R. A. Briceño, *Phys. Rev. D* **89**, 074507 (2014).
- [29] R. A. Briceño, Z. Davoudi, and T. C. Luu, *Phys. Rev. D* **88**, 034502 (2013).
- [30] M. Gockeler, R. Horsley, M. Lage, U. G. Meissner, P. E. L. Rakow, A. Rusetsky, G. Schierholz, and J. M. Zanotti, *Phys. Rev. D* **86**, 094513 (2012).
- [31] M. T. Hansen and S. R. Sharpe, *Phys. Rev. D* **86**, 016007 (2012).
- [32] S. He, X. Feng, and C. Liu, *J. High Energy Phys.* **07** (2005) 011.
- [33] R. A. Briceño, M. T. Hansen, S. R. Sharpe, and A. P. Szczepaniak, *Phys. Rev. D* **100**, 054508 (2019).
- [34] A. W. Jackura, R. A. Briceño, S. M. Dawid, M. H. E. Islam, and C. McCarty, *Phys. Rev. D* **104**, 014507 (2021).
- [35] M. T. Hansen, F. Romero-López, and S. R. Sharpe, *J. High Energy Phys.* **07** (2020) 047; **02** (2021) 14(E).
- [36] M. T. Hansen, F. Romero-López, and S. R. Sharpe, *J. High Energy Phys.* **04** (2021) 113.
- [37] V. Bernard, M. Lage, U.-G. Meissner, and A. Rusetsky, *J. High Energy Phys.* **08** (2008) 024.
- [38] D. Ronchen, M. Doring, F. Huang, H. Haberzettl, J. Haidenbauer, C. Hanhart, S. Krewald, U. G. Meissner, and K. Nakayama, *Eur. Phys. J. A* **49**, 44 (2013).
- [39] C. Morningstar, J. Bulava, B. Fahy, J. Foley, Y. Jhang, K. Juge, D. Lenkner, and C. Wong, *Phys. Rev. D* **88**, 014511 (2013).
- [40] PLEGMA Development Group, PLEGMA software package (2020–2022), <https://github.com:cylqcd/PLEGMA>.
- [41] S. Gusken, U. Low, K. H. Mutter, R. Sommer, A. Patel, and K. Schilling, *Phys. Lett. B* **227**, 266 (1989).
- [42] M. Albanese *et al.* (APE Collaboration), *Phys. Lett. B* **192**, 163 (1987).
- [43] C. Alexandrou *et al.*, *Phys. Rev. D* **98**, 054518 (2018).
- [44] M. Luscher and U. Wolff, *Nucl. Phys.* **B339**, 222 (1990).
- [45] B. Blossier, M. Della Morte, G. von Hippel, T. Mendes, and R. Sommer, *J. High Energy Phys.* **04** (2009) 094.
- [46] M. Fischer, B. Kostrzewa, J. Ostmeier, K. Ottnad, M. Ueding, and C. Urbach, *Eur. Phys. J. A* **56**, 206 (2020).
- [47] M. R. Osborne and G. K. Smyth, *SIAM J. Sci. Comput.* **16**, 119 (1995).
- [48] C. Alexandrou, T. Leontiou, C. N. Papanicolas, and E. Stiliaris, *Phys. Rev. D* **91**, 014506 (2015).
- [49] C. Alexandrou, J. Berlin, M. Dalla Brida, J. Finkenrath, T. Leontiou, and M. Wagner, *Phys. Rev. D* **97**, 034506 (2018).
- [50] C. Alexandrou, J. Berlin, J. Finkenrath, T. Leontiou, and M. Wagner, *Phys. Rev. D* **101**, 034502 (2020).
- [51] J. Bulava, B. Fahy, B. Hörz, K. J. Juge, C. Morningstar, and C. H. Wong, *Nucl. Phys.* **B910**, 842 (2016).
- [52] M. Fischer, B. Kostrzewa, M. Mai, M. Petschlies, F. Pittler, M. Ueding, C. Urbach, and M. Werner (Extended Twisted Mass (ETM) Collaboration), *Phys. Lett. B* **819**, 136449 (2021).
- [53] E. T. Neil and J. W. Sitison, arXiv:2208.14983.
- [54] M. Hoferichter, J. Ruiz de Elvira, B. Kubis, and U.-G. Meißner, *Phys. Rep.* **625**, 1 (2016).
- [55] M. Hoferichter, J. Ruiz de Elvira, B. Kubis, and U.-G. Meißner, *Phys. Rev. Lett.* **115**, 192301 (2015).
- [56] M. Hoferichter, J. Ruiz de Elvira, B. Kubis, and U.-G. Meißner, *Phys. Rev. Lett.* **115**, 092301 (2015).
- [57] C. Ditsche, M. Hoferichter, B. Kubis, and U. G. Meissner, *J. High Energy Phys.* **06** (2012) 043.
- [58] M. Hoferichter, J. R. de Elvira, B. Kubis, and U.-G. Meißner, *Phys. Lett. B* **843**, 138001 (2023).
- [59] P. C. Bruns, M. Mai, and U. G. Meissner, *Phys. Lett. B* **697**, 254 (2011).
- [60] J. Ruiz de Elvira, M. Hoferichter, B. Kubis, and U.-G. Meißner, *J. Phys. G* **45**, 024001 (2018).
- [61] G. Höhler, *Methods and Results of Phenomenological Analyses/Methoden und Ergebnisse phänomenologischer Analysen*, Vol. 9b2 of Landolt-Boernstein—Group I

- Elementary Particles, Nuclei and Atoms (Springer, New York, 1983), ISBN 978-3-540-11282-2, 978-3-540-39059-6.
- [62] R. L. Workman *et al.* (Particle Data Group), *Prog. Theor. Exp. Phys.* **2022**, 083C01 (2022).
- [63] www.gauss-centre.eu.
- [64] S. Kesselheim, A. Herten, K. Krajsek, J. Ebert, J. Jitsev, M. Cherti, M. Langguth, B. Gong, S. Stadler, A. Mozaffari *et al.*, JUWELS booster—A supercomputer for large-scale AI research, [arXiv:2108.11976](https://arxiv.org/abs/2108.11976).
- [65] G. Endrodi, *Comput. Phys. Commun.* **182**, 1307 (2011).